A STUDY OF PRE-FLARE SOLAR CORONAL MAGNETIC FIELDS: MAGNETIC FLUX ROPES

Aiying Duan [1*], Chaowei Jiang [2*], Wen He [2], Xueshang Feng [3], Peng Zou [2], Jun Cui [1,4]

[1] School of Atmospheric Sciences, Sun Yat-sen University, Zhuhai 519000, China

[2] Institute of Space Science and Applied Technology, Harbin Institute of Technology, Shenzhen 518055, China

[3] SIGMA Weather Group, State Key Laboratory for Space Weather, National Space Science Center, Chinese Academy of Sciences, Beijing 100190, China

[4] CAS Center for Excellence in Comparative Planetology, China

ABSTRACT

Magnetic flux ropes (MFRs) are thought to be the central structure of solar eruptions, and their ideal MHD instabilities can trigger the eruption. Here we performed a study of all the MFR configurations that lead to major solar flares, either eruptive or confined, from 2011 to 2017 near the solar disk center. The coronal magnetic field is reconstructed from observed magnetograms, and based on magnetic twist distribution, we identified the MFR, which is defined as a coherent group of magnetic field lines winding an axis with more than one turn. It is found that 90% of the events possess pre-flare MFRs, and their three-dimensional structures are much more complex in details than theoretical MFR models. We further constructed a diagram based on two parameters, the magnetic twist number which controls the kink instability (KI), and the decay index which controls the torus instability (TI). It clearly shows lower limits for TI and KI thresholds, which are $n_{\rm crit} = 1.3$ and $|T_w|_{\rm crit} = 2$, respectively, as all the events above $n_{\rm crit}$ and nearly 90% of the events above $|T_w|_{\rm crit}$ erupted. Furthermore, by such criterion, over 70% of the events can be discriminated between eruptive and confined flares, and KI seems to play a nearly equally important role as TI in discriminating between the two types of flare. There are more than half of events with both parameters below the lower limits, and 29% are eruptive. These events might be triggered by magnetic reconnection rather than MHD instabilities.

Keywords: Magnetic fields; Magnetohydrodynamics (MHD); Methods: numerical; Sun: corona; Sun: flares

1. INTRODUCTION

As a leading cause of space weather, solar eruptions, including flares and coronal mass ejections (CMEs) are still difficult to predict. Now it is commonly believed that solar eruptions have their root in the evolution of magnetic field in the solar atmosphere. In particular, the magnetic field dominates the dynamics in the solar corona, which is a highly electric-conducting plasma environment. However, two key questions arise in understanding the physics of solar eruptions: what is magnetic structure of the corona before eruption and what is the triggering mechanism of the eruption? Observations show that major flares are often associated with CMEs, but many flares do not, which are named as confined flares. Thus another important question is what is the factor that determines such difference?

Through several decades of studies, a variety of models have been proposed to answer these questions (e.g., see review papers of Forbes et al. 2006; Shibata & Magara 2011; Aulanier 2014; Schmieder & Aulanier 2012; Schmieder et al. 2013; Janvier et al. 2015). In a rough classification, these models fall into two categories, one is based on magnetic reconnection (Mikic & Linker 1994; Antiochos et al. 1999; Moore et al. 2001) and the other is ideal MHD instabilities (Bateman 1978; Hood & Priest 1981; Török et al. 2004; Török & Kliem 2005; Kliem & Török 2006; Fan & Gibson 2007; Aulanier et al. 2010). In the former group, there are two models most frequently invoked, namely the runaway tether-cutting reconnection (Moore et al. 2001) and the breakout reconnection (Antiochos et al. 1999). Both these models assume the pre-flare magnetic field as a strongly sheared configuration with a topology prone to reconnection, and an eruption will occur if a positive feedback between the reconnection and the outward expansion of the sheared magnetic flux can be established. In the tether-cutting model, internal reconnection between the sheared magnetic arcades triggers the eruption, while in the breakout model, reconnection takes place externally, above or aside of the sheared arcades in a magnetic null point topology. However, in what conditions the feedback can be triggered is still elusive.

In the ideal MHD models, two kinds of ideal instabilities are most extensively investigated in the context of solar eruptions, which are the helical kink instability (KI, Hood & Priest 1981; Török et al. 2004; Török & Kliem 2005; Török et al. 2010) and the torus instability (TI, Kliem & Török

*Corresponding authors:
duanaiy@mail.sysu.edu.cn; chaowei@hit.edu.cn

2006). Both of the two instabilities are developed based on a fundamental magnetic configuration in the plasma known as magnetic flux rope (MFR) (Kuperus & Raadu 1974; Chen 1989; Titov & Démoulin 1999; Amari et al. 2014), which is a coherent group of twisted magnetic flux that winding around a common axis. Naturally in models of the ideal MHD instabilities, MFR must exist in the corona prior to an eruption, and evolution in the photosphere can then, often slowly, build up the MFR to an unstable regime and produce the eruption. From a theoretical point of view, the existence of pre-eruptive MFRs should be common in the corona. This is because the coronal magentic field is approximately force-free such that the electric currents direct dominantly along magnetic field lines, thus such field-aligned currents introduce poloidal magnetic flux around the currents, which has a potential to make the field lines twist and form MFRs. Indeed, the relevance of MFRs with solar flares and eruptions has also been extensively evidenced from both observations and coronal magnetic field reconstructions. For instance, X-ray and EUV sigmoid, filament, EUV hot channel, and coronal cavity are invoked as indirect observations of coronal MFRs (e.g., see a recent review paper by Cheng et al. 2017). Using nonlinear force-free field (NLFFF) extrapolations from vector magnetograms, which is a basic tool for unraveling the 3D information of solar coronal magnetic field, MFRs were identified frequently (e.g., see another recent review by Guo et al. 2017).

The trigger of MFR eruption can be through either KI or TI, basing mainly on two critical parameters. KI is controlled by the twist degree of MFR, occurring if the twist of the MFR exceeds a critical value. Through a eruptive expansion, KI will transform the excessive magnetic twist to a writhe through a helical deformation of the MFR axis. Theoretical and numerical investigations have shown that the KI threshold, as measured by the winding number of magnetic field lines around the MFR's axis, seems to have a wide range from ~ 1.25 turns to ~ 2.5 turns (Baty 2001; Fan & Gibson 2003; Török & Kliem 2003; Török et al. 2004; Török & Kliem 2005), which depends on the details of the MFR, such as the geometry of the axis, the aspect ratio of the MFR (i.e., ratio of length of the rope to the size of its cross section), and the line-tying effects by the photosphere. On the other hand, TI is controlled by the decay index (Török & Kliem 2005, 2007; Kliem & Török 2006), which is the spatial deceasing speed of the MFR's overlying magnetic field that strapping the MFR. Assuming a outward quasi-static expansion of the MFR due to its hoop force, which is resulted by the self-inductive effect of the current in the MFR, both the hoop force and the strapping force will decrease with the expansion. If the strapping force decreases faster than the hoop force, the system will be unstable because the net force points to the direction of expansion. The TI threshold of decay index is found to have typical values in the domain of $1.1 \sim 1.7$, again derived from a series of theoretical and nu-

merical investigations (Kliem & Török 2006; Török & Kliem 2007; Fan & Gibson 2007; Aulanier et al. 2010; Démoulin & Aulanier 2010; Fan 2010; Olmedo & Zhang 2010; Zuccarello et al. 2015). An attractive advantage of these ideal MHD models is that the controlling parameters, e.g., the twist degree of the MFR and the decay index of the strapping field, can be used potentially in forecasting the eruptiveness of flares.

The theory of KI and TI has been recently, and is becoming even more widely, applied to study real solar eruptions. Case studies of solar eruptions using NLFFF reconstructions often shows MFRs exist prior to flare and its ensuing eruption is very likely due to KI (e.g., Liu et al. 2016) or TI (e.g., Cheng et al. 2013; Jiang et al. 2013; Jiang et al. 2018), as the reconstructed MFRs appears to be close to the thresholds. However, due to the intrinsic complexity of the magnetic field in the solar corona, the configuration of MFRs can be very different from case to case, and cannot be fully characterized by the KI and TI theory, which are both based on relatively simplified or idealized configuration. Furthermore, a recent laboratory experiment of MFRs emulating the dynamic behaviors of solar line-tied MFRs suggests that the theory might miss including the magnetic tension force caused by the toroidal magnetic flux of the rope (Myers et al. 2015). If such magnetic tension is strong enough, i.e., the toroidal flux is large enough (and thus corresponding to a sufficiently small magnetic twist), it can restrict the flux rope from eruption even it fulfills the TI condition, for which the authors call it as a 'failed torus' event. Thus the application of the theoretical parameters of KI and TI is still not straightforward.

A very recent statistic study of the controlling parameters of KI and TI for solar flares was performed by Jing et al. (2018). They surveyed 38 major flares, including 26 ejective and 12 confined ones, by NLFFF reconstructions of the pre-flare coronal magnetic field using a code developed by Wiegelmann (2004). Then for each events, the reconstructed 3D magnetic field is analyzed by computing the magnetic twist and decay index. It was found that the KI parameter, i.e., the twist number appears to play no role in discriminating between the confined and eruptive events. And for the TI parameter, the threshold of decay index is found to be ~ 0.75, which is much lower than the typical values that are derived in theoretical and numerical studies. However, as also pointed out by the authors, such results might strongly depends on the quality or reliability of the coronal magnetic field reconstructions. Currently there are many methods available for NLFFF extrapolations from the vector magnetograms, but different methods seem to produce rather inconsistence results between each other (e.g., DeRosa et al. 2009; Régnier 2013; Aschwanden et al. 2014; Duan et al. 2017; Wiegelmann et al. 2017). Thus any results based on any single NLFFF code must be taken with cautions, and independent studies with different codes are required for a better inspection. Thus, one of the purposes of this paper is to

see how the results behave if using an independent NLFFF code to perform a similar statistical investigation. The other purpose is, for the first time, to statistically investigate the complexity of the pre-flare coronal MFRs.

In this paper, we employed the coronal magnetic field reconstruction method developed by Jiang & Feng (2013), named the CESE–MHD–NLFFF code, to study a slightly larger sample of 45 major flares with 29 eruptive and 16 confined. We attempt to reveal the complexity of MFRs in solar corona by showing the magnetic configuration of each MFR. With a much stricter definition of MFR and a more relevant way of calculating the decay index, our study shows that the KI and TI parameters play an equal important role in discriminating between the eruptive and confined events, and the TI thresholds for the eruptive events is much closer to the theory. The rest of the paper is organized as follows: Data and method are presented in Section 2, then results are given in Section 3, and finally discussions and conclusions are made in Section 4.

2. METHOD

2.1. *Event Selection*

Since we are interested in the major flares for which coronal magnetic field extrapolation can be perform with reliable observed magnetograms, we use the similar criterion for selecting events samples as employed in Toriumi et al. (2017) and Jing et al. (2018). That is all the flares above GOES-class M5 (in general) that occurred within 45 degree of the solar disk center from 2011 January to 2017 December, and most of them occurred in active regions (ARs). For the confined flares, the flare class criterion is relaxed to include also M3.9. Furthermore, since some ARs (e.g., AR12673) produced several (more than three) flares fulfilling the above criterion, we select only two flares to avoid the over-representation for a certain AR: the first one is the largest flare, and the second one is the flare occurring nearest to the disk center. But if these two flares are both eruptive and meanwhile the AR also produced one or more confined flares, we replace the second one with the confined flare (the largest one if there are more than one confined flares). There are 45 events in total, including 29 eruptive flares and 16 confined flares from 30 different ARs, as listed in Table 1. Note that two events (number 24 and 30) are inter-AR flares.

2.2. *Coronal Magnetic Field Reconstructions*

For each event, we carried out 3D magnetic field reconstruction for the pre-flare corona from the *SDO*/HMI vector magnetograms using the CESE–MHD–NLFFF code (Jiang & Feng 2013). The last available magnetogram for at least 10 minutes before the flare GOES start time is used to avoid the possible artifacts introduced by the strong flare emission. In particular, we used the data product of the Space-weather HMI Active Region Patch (SHARP, Bobra et al. 2014), in which the 180° ambiguity has been resolved by

using the minimum energy method, the coordinate system has been modified via the Lambert method, and the projection effect has been corrected. The CESE–MHD–NLFFF model is based on an MHD-relaxation method which seeks approximately force-free equilibrium. It solves a set of modified zero-β MHD equations with a friction force using an advanced conservation-element/solution-element (CESE) space-time scheme on a non-uniform grid with parallel computing (Jiang et al. 2010). The code also utilizes adaptive mesh refinement and a multi-grid algorithm to optimize the relaxation process. This model has been tested by different benchmarks including a series of analytic force-free solutions (Low & Lou 1990) and numerical MFR models (Titov & Démoulin 1999). The results of extrapolation reproduced from *SDO*/HMI are in good agreement with corresponding observable features like filaments, coronal loops, and sigmoids (Jiang & Feng 2013; Jiang et al. 2014).

2.3. *Magnetic Twist Number and Identification of MFRs*

It is nontrivial to identify MFRs in a reconstructed coronal magnetic field because their configuration are generally complex compared with theoretical models. Here the search of MFR is based on the distribution of a parameter called magnetic twist number (Berger & Prior 2006), which can be conveniently computed without resorting to the geometry of an MFR (Liu et al. 2016). The magnetic twist number T_w for a given (closed) field line is defined as

$$T_w = \int_L \frac{(\nabla \times \mathbf{B}) \cdot \mathbf{B}}{4\pi B^2} dl \qquad (1)$$

where the integral is taken along the length L of the magnetic field line from one footpoint on the photosphere to the other. As shown by Liu et al. (2016), T_w provides an good approximation of the number of turns that two infinitesimally close field lines wind about each other. Thus T_w is not identical to the classic winding number of field lines about a common axis, the parameter often used in the analysis of the helical KI. Nevertheless, according to Liu et al. (2016)'s analysis, the magnetic field line that possesses the extremum value (maximum or minimum) of $|T_w|$ in an MFR can be reliably regarded as the rope axis, and T_w computed in the vicinity of the axis approaches the winding number. For each 3D reconstructed magnetic field data, we compute the twist number on grid points with a resolution 4 times of the original data, from which a 3D smooth distribution of T_w is obtained. Basing on this distribution of T_w, the MFR in the field can be precisely identified.

There is no accurate definition of solar coronal MFR in the literature. Generally, an MFR refers to a group of magnetic field lines spiraling around the same axis with certain twist, but there seems to be no consensus on what extent of the twist degree can be regarded as a rope. Here we follow the definition of Liu et al. (2016), that is, the MFR is defined as a coherent group of magnetic field lines with $|T_w| \geq 1$

Table 1. List of events and properties of their MFRs.

No.	Flare peak time	Flare class	NOAA AR	Position	E/C[a]	T_w	n
1	SOL2011-02-13T17:38	M6.6	11158	S20E04	E	0.76	0.99
2	SOL2011-02-15T01:56	X2.2	11158	S20W10	E	1.52	0.98
3	SOL2011-03-09T23:23	X1.5	11166	N08W09	C	-1.75	0.50
4	SOL2011-07-30T02:09	M9.3	11261	S20W10	C	-0.88	0.51
5	SOL2011-08-03T13:48	M6.0	11261	N16W30	E	2.45	1.40
6	SOL2011-09-06T01:50	M5.3	11283	N14W07	E	0.92	0.52
7	SOL2011-09-06T22:20	X2.1	11283	N14W18	E	1.02	1.65
8	SOL2011-10-02T00:50	M3.9	11305	N12W26	C	-0.92	0.42
9	SOL2012-01-23T03:59	M8.7	11402	N28W21	E	-1.63	0.73
10	SOL2012-03-07T00:24	X5.4	11429	N17E31	E	-2.11	0.71
11	SOL2012-03-09T03:53	M6.3	11429	N15W03	E	-1.17	0.73
12	SOL2012-05-10T04:18	M5.7	11476	N12E22	C	-1.11	1.21
13	SOL2012-07-02T10:52	M5.6	11515	S17E08	E	-1.56	0.35
14	SOL2012-07-05T11:44	M6.1	11515	S18W32	C	1.14	-0.41
15	SOL2012-07-12T16:49	X1.4	11520	S15W01	E	2.20	0.42
16	SOL2013-04-11T07:16	M6.5	11719	N09E12	E	-1.10	0.26
17	SOL2013-10-24T00:30	M9.3	11877	S09E10	E	2.00	0.56
18	SOL2013-11-01T19:53	M6.3	11884	S12E01	C	1.50	0.42
19	SOL2013-11-03T05:22	M4.9	11884	S12W17	C	3.00	0.07
20	SOL2013-11-05T22:12	X3.3	11890	S12E44	E	1.35	2.72
21	SOL2013-11-08T04:26	X1.1	11890	S12E13	E	1.26	1.87
22	SOL2013-12-31T21:58	M6.4	11936	S15W36	E	-2.20	1.11
23	SOL2014-01-07T10:13	M7.2	11944	S13E13	C	1.65	0.21
24[*]	SOL2014-01-07T18:32	X1.2	11944	S15W11	E	6.50	0.20
25	SOL2014-02-02T09:31	M4.4	11967	S10E13	C	-1.73	-0.12
26	SOL2014-02-04T04:00	M5.2	11967	S14W06	C	-1.90	1.03
27	SOL2014-03-29T17:48	X1.1	12017	N10W32	E	1.53	1.72
28	SOL2014-04-18T13:03	M7.3	12036	S20W34	E	2.30	1.82
29	SOL2014-09-10T17:45	X1.6	12158	N11E05	E	-0.85	0.17
30[*]	SOL2014-09-28T02:58	M5.1	12173	S13W23	E	-2.76	1.96
31	SOL2014-10-22T14:28	X1.6	12192	S14E13	C	-1.10	0.94
32	SOL2014-10-24T21:41	X3.1	12192	S22W21	C	-1.79	0.64
33	SOL2014-11-07T17:26	X1.6	12205	N17E40	E	3.55	1.21
34	SOL2014-12-04T18:25	M6.1	12222	S20W31	C	2.60	0.60
35	SOL2014-12-17T04:51	M8.7	12242	S18E08	E	0.70	0.66
36	SOL2014-12-18T21:58	M6.9	12241	S11E15	E	1.09	1.49
37	SOL2014-12-20T00:28	X1.8	12242	S19W29	E	1.32	0.56
38	SOL2015-03-11T16:21	X2.1	12297	S17E22	E	2.04	1.80
39	SOL2015-03-12T14:08	M4.2	12297	S15E06	C	1.10	0.72
40	SOL2015-06-22T18:23	M6.5	12371	N13W06	E	-1.24	1.51
41	SOL2015-06-25T08:16	M7.9	12371	N12W40	E	-2.90	0.49
42	SOL2015-08-24T07:33	M5.6	12403	S14E00	C	1.04	0.33
43	SOL2015-09-28T14:58	M7.6	12422	S20W28	C	-1.25	1.20
44	SOL2017-09-04T20:33	M5.5	12673	S10W11	E	-1.43	1.09
45	SOL2017-09-06T12:02	X9.3	12673	S09W34	E	-1.80	1.72

[a] E–eruptive, C–confined.

[*] Event 24 occurred between NOAA ARs 11944 and 11943, and event 30 occurred between ARs 12173 and 12172.

(i.e., field lines spiral above a full turn) and with the same sign of twist. The coherence means that the volume of the magnetic flux with $|T_w| \geq 1$ forms a single tube without segmentation. In some events, there are more than one MFR as the magnetic flux with $|T_w| \geq 1$ forms multiple, separate tubes, and even more complex, different MFRs can have inverse signs of twist from each other (which will be shown in Section 3), indicating the intrinsic complexity of the coronal magnetic field. There are places where the $|T_w|$ is strong, but forms a sheet like structure with width close to the grid size. These structures are actually complex magnetic separatrix layers or quasi-separatrix layers and cannot be defined as MFR, although their twist numbers appear large. The reason which makes the $|T_w|$ high is the relatively high value of J/B in these regions. We exclude these regions in searching flux rope. Furthermore, the search of MFR is aid by *SDO*/AIA observations such that the MFR is restricted within the flare site, and especially the morphology of the MFR is compared with pre-eruptive filaments if they are observable. As an example, in Figure 1, we show the MFR in the 45th event, which is the pre-flare magnetic field of the largest X-class flare in AR 12673, also the largest one of solar cycle 24 (Sun & Norton 2017; Inoue et al. 2018; Liu et al. 2018; Mitra et al. 2018; Seaton & Darnel 2018; Wang et al. 2018; Getling 2019; Petrie 2019). Clearly the MFR is identified by a volumetric channel with $|T_w| \geq 1$ and strong current density. The MFR body appears roughly to be a C shape following the main PIL of the AR.

2.4. *KI Parameter*

By a comprehensive study of the magnetic twist distribution and evolution in an AR that produced a series of flares, Liu et al. (2016) suggests that the magnetic field line with maximum twist number in their studied MFR is a reliable proxy of the rope axis. Further, they found that, comparing to other parameters like magnetic energy and helicity, the maximum twist number changes most prominently across the flares, as it increases systematically before each flare and decrease stepwise after it. This suggests that the MFR's maximum twist number, $|T_w|_{max}$, is very sensitive in association with KI occurring in flares. We thus employed the $|T_w|_{max}$ in our analysis as the KI controlling parameter.

After locating the MFRs, we can then locate their axis, which is defined as a single field line that possesses the maximum value of the twist number, $|T_w|_{max}$, in the MFR. As shown in Figure 1, the axis of the rope is the field lines with largest twist of $|T_w| = 1.8$. It is fully wrapped by the isosurface of $|T_w| = 1$, running horizontally in the central part and reaching a height of roughly 20 arcsec. The location of the axis is double checked by using vertical slices cutting through the rope axis in a perpendicular direction and to see if the poloidal flux of the rope forms rings centered at the axis in such cross section, as shown in Figure 1(f). This is fulfilled for most of the events, suggesting that the field line

with maximum T_w is a reliable proxy of the rope axis, which is consistent with the findings of Liu et al. (2016).[1] For those events that possess multiple MFRs, axis for each one can be identified independently. There are complex cases in which the field line with $|T_w|_{max}$ in the MFR can runs partly on the surface of the rope, because of the unevenly distribution of the twist number.

2.5. *TI Parameter*

In many literatures, the decay index is simply defined as

$$n = -\frac{d\log(B)}{d\log(h)} \qquad (2)$$

where B denotes the strapping field stabilizing the MFR and h is the vertical height locally or radial distance globally, assuming that the MFR erupts vertically or radially and the strapping force point in the opposite direction. However, since the triggering and initiation of MFR eruption is strongly influenced by its complex magnetic environment in the lower corona, which is often non-symmetric with respect to the PIL such that the eruption direction is not along the vertical (or radial) direction. Such non-radial eruptions are frequently observed in filament eruptions (McCauley et al. 2015). In such case, computing the decay index along an oblique line matching the eruption direction ought to be more accurate. As illustrated in Figure 2, the MFR is significantly inclined to the right side away from the vertical direction, owing to the stronger magnetic flux distribution (and thus the magnetic pressure) in the left side. To define the decay index in such configuration, we first use a vertical slice cutting through the middle of the rope, generally, at the apex of the axis (i.e., highest point on the axis, marked as P in the Figure), in perpendicular direction to the rope axis. The intersection point of the bottom PIL with the slice is marked as O as shown in the Figure. Then, we calculate decay index in the OP direction with O as the starting point. As usual, the potential field model extrapolated from the B_z component of the photospheric magnetogram can be considered as a good approximation of the external (strapping) magnetic field with respect to the MFR. To be more relevant, we further decompose the potential field into three orthogonal components B_e, B_p, and B_t, where B_e is along OP, B_p is perpendicular to the OP on the slice, and B_t is perpendicular to the slice. In defining n we only use the poloidal flux B_p, that is

$$n = -\frac{d\log(B_p)}{d\log(r)} \qquad (3)$$

(where r is the distance pointing from O to P). This is because the cross product of the current of the rope (which is along the axis) with only the poloidal flux of the overlying field can

---

[1] It should be noted that there are cases in which the MFR axis is located at a local minimum of $|T_w|$, especially in decayed active regions and the quiet Sun (e.g., Su et al. 2011).
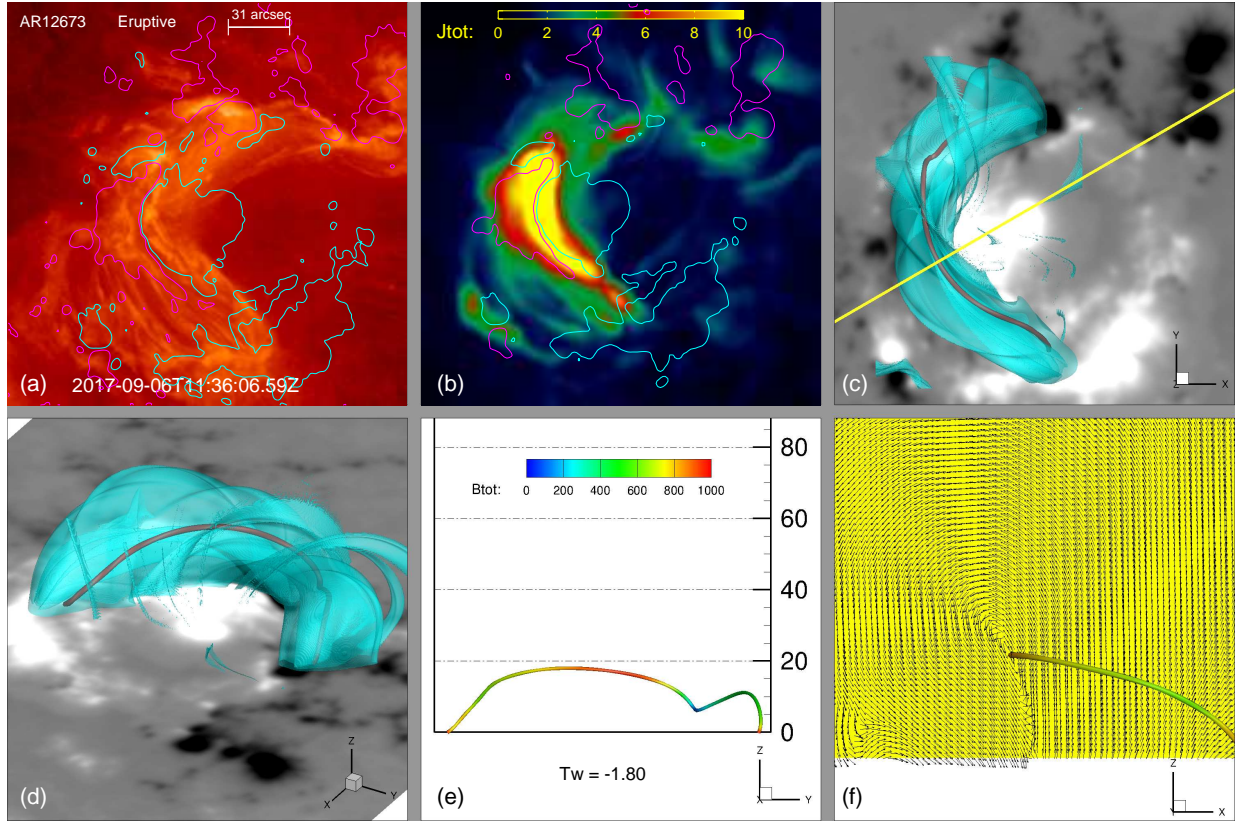
Figure 1. An example showing the identification of MFR. The figure shows the 45th event, i.e., the pre-flare magnetic field of the X9.3 flare in AR 12673. (a) *SDO*/AIA 304 Å image of the pre-flare corona. (b) A vertical integration of the current density derived from the reconstructed magnetic field, showing the strong-current region. (c) The cyan, transparent object is the iso-surface of the $|T_w| = 1$ and the red, thick line represent the magnetic field line possessing the maximum value of $|T_w|$, which is regarded as the axis of the MFR. (d) The same structure of (c) but in a different angle of view in 3D. (e) Side view of the rope axis with colors denote the magnetic field strength on the line. The unit of the z axis is 1 arcsec (or 720km). (f) A central vertical cross section of the MFR whose location is dented by the yellow line in panel (c), with the transverse field on the slice shown by the arrows, which forms spirals centered at the axis of the rope denoted by the thick line.

produce the strapping force (directing P to O) that stabilizing the MFR. The other components, for example, B_t is parallel to the current and has no effect, and the cross product of current with B_e produce a force parallel to the B_p which only controls the eruption direction and furthermore B_e is often small.

3. RESULTS

3.1. *Complex Configurations*

With our strict definition, only 6 of the 45 events (13%) have no MFR as the maximum twist number $|T_w|_{\max}$ is less than 1 (although they are very close to 1). For the remaining 39 events, we plot the MFR configurations in the figures from Figure 3 to Figure 9. For each event, three different angles of view are shown and a *SDO*/AIA-304 Å image taken at the same time used for reconstructions is present for comparison. Overall, the twist flux forms coherently ropes and the central section of the ropes run roughly along the main PIL of the AR, but the shapes are very different from case to case and it is not easy to make classification for them. Furthermore, from the morphology, very few of them show an idealized, symmetric half-circle MFR that is often used for theoretical

study, which indicates that the complexity of coronal MFRs is far beyond the characterization by current theoretical (or idealized) models. The aspect ratios of the MFRs are also different, some are rather short and thick, while some are long and thin. Many MFRs have a serpent shape that its body touch the bottom surface one or several times (for instance, see events 10, 15, 18, etc.), suggesting there are bald patches along the PIL below the MFRs. Most of the MFRs show good coherence except a few of them are disturbed by segmented sheet-like structures of $|T_w| > 1$ locating very close to them. Nevertheless, the comparison of the MFR structures and the corresponding AIA images shows good agreement between the filaments and the MFRs. Almost for each MFR, a filament can be identified in the AIA 304 Å channel, and the spine of the filament looks co-spatial to the axis of the MFRs. Only in the events 16, 20, 25, and 43, there appears to be no filament co-spatial to the MFRs. Note that in event 24, the filament is not clearly seen in AIA 304 Å but a co-spatial filament channel can be seen if check the AIA 171 Å images (not shown here).

Although the majority of the events has a single MFR, there are cases in which we identified two MFRs in a single
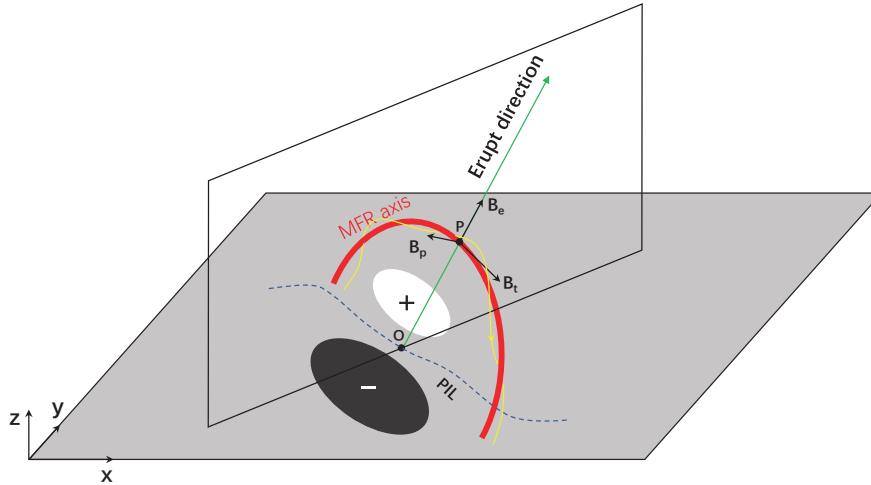
Figure 2. Illustration of calculating the decay index n at the apex of the MFR axis. The thick red curve is the MFR axis, and P denotes the highest point along the axis. A vertical slice cutting perpendicularly through the axis at P. The intersection of the vertical slice with the main PIL is marked as O. The background magnetic field **B**, which is computed based on the potential field model, are decomposed into three components as B_e, B_p, and B_t.

event (events 3, 5, 9, 30, 31, 32) or even three MFRs (events 36 and 40)[2]. So in total the events with multiple-MFR configuration accounts for 20% of all the events (8 in 39). Actually the multiple-MFR configuration is even more common in the ARs if we release the restriction on only those relevant to the flare site. For some events, for instance, number 36 and 40, there might be no difference in magnetic topology between different flux ropes in the multiple-MFRs configuration, and only the uneven distribution of magnetic twist causes the complexity of the MFR system. It is worth noting that the two MFRs in events 31 and 32, which are both confined X-class flares from the largest region AR 12192 (Sun et al. 2015; Jiang et al. 2016), have inverse signs of magnetic twist. This might provide an interesting explanation why these flares are confined, as the inverse helicity contents of the MFRs might cancel with each other during the flare such that there is no need for the pre-flare reserved helicity to release out of the AR through eruption, and further investigations on these events will be performed in future study.

In Figure 10, we show the distribution of the $|T_w|_{\max}$ for all the events. We find the average $|T_w|_{\max}$ of 1.73 and the median value of 1.52, and 13 events (29%) have $|T_w|_{\max}$ larger than 2. Previous NLFFF reconstructions for pre-eruptive or quiescent filaments often yields weakly twisted MFRs with

twist number mostly below 1.5 (Liu et al. 2016; Wang et al. 2016). Comparing with previous results, we find that our extrapolations can reconstruct relatively high twisted flux rope. In all cases, the largest number reaching 6.5 in the event 24, which is an X1.2 flare occurring between ARs 11944 and 11943, and by checking the AIA images, we found that the flux rope for this event actually corresponds to an intermediate filament channel between the two ARs, and its flare eruption is most likely caused by KI due to the strong magnetic twist.

3.2. *TI versus KI parameter diagram*

In Figure 11(a), we show the scatter diagram of decay index n (TI parameter) versus the $|T_w|_{\max}$ (KI parameter) for all the 45 events. For the 6 non-MFR cases, we also calculated their $|T_w|_{\max}$ and the decay index n of the field line with $|T_w|_{\max}$ (shown in green color). From the distribution of eruptive and confined flares in the parameter space, it can be empirically identified a critical value for n and $|T_w|$, which are $n_{\mathrm{crit}} = 1.3$ and $|T_w|_{\mathrm{crit}} = 2$, respectively, as marked on the figure. According to these critical values, the distribution of the events falls into four quadrants which are defined as: Q1 ($n >= 1.3$ and $|T_w| >= 2$), Q2 ($n >= 1.3$ and $|T_w| < 2$), Q3 ($n < 1.3$ and $|T_w| < 2$), and Q4 ($n < 1.3$ and $|T_w| >= 2$). The histograms for events falling into different quadrants are shown in Figure 11(b) and (c). As can be seen in the Figure, all the events with decay index above n_{crit} (i.e., in Q1+Q2) erupted. Thus $n > n_{\mathrm{crit}}$ can be regarded as a sufficient condi-

---

[2] Note that for such multiple MFR cases, only the MFR with the largest height is listed in Table 1 and used in the statistic analysis.
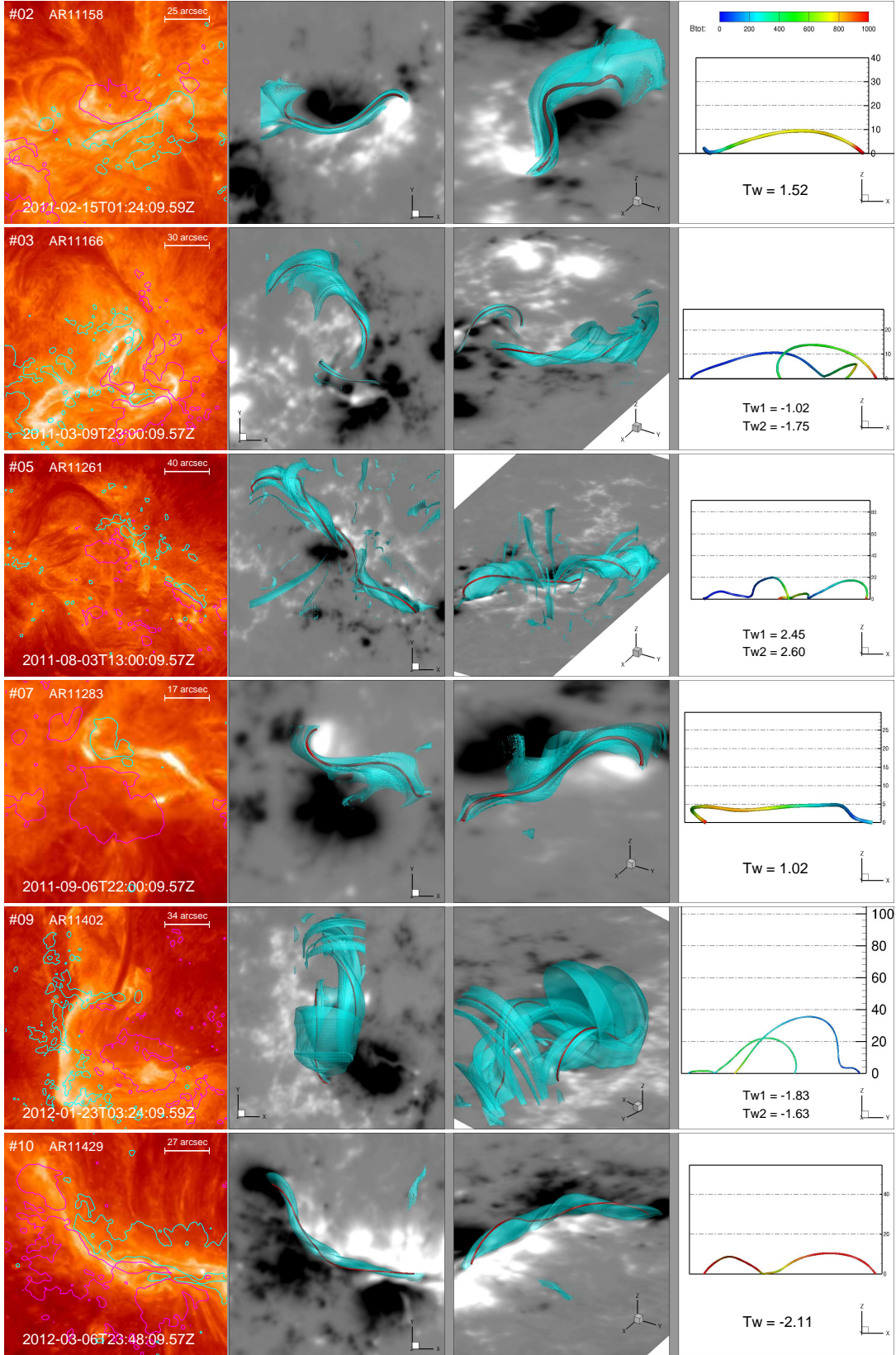
Figure 3. Configuration of the MFRs. From the left to right are *SDO*/AIA 304 Å image taken at the pre-flare time, the reconstructed MFR structure in three different views. In the AIA images, contour lines of photosphere $B_z = \pm 1000$ Gauss are overlaid. In the middle panels, the 3D transparent structures colored in cyan are iso-surface of $|T_w| = 1$, while the thick red lines denote the axis of the MFRs. The background is shown with photosphere magnetogram (saturated at ± 1000 Gauss). In the right panels, only the MFR's axis is shown with color denotes the magnetic field strength along the rope axis. For each rope axis, the twist number T_w is shown. The unit of the z axis is 1 arcsec (or 720km).
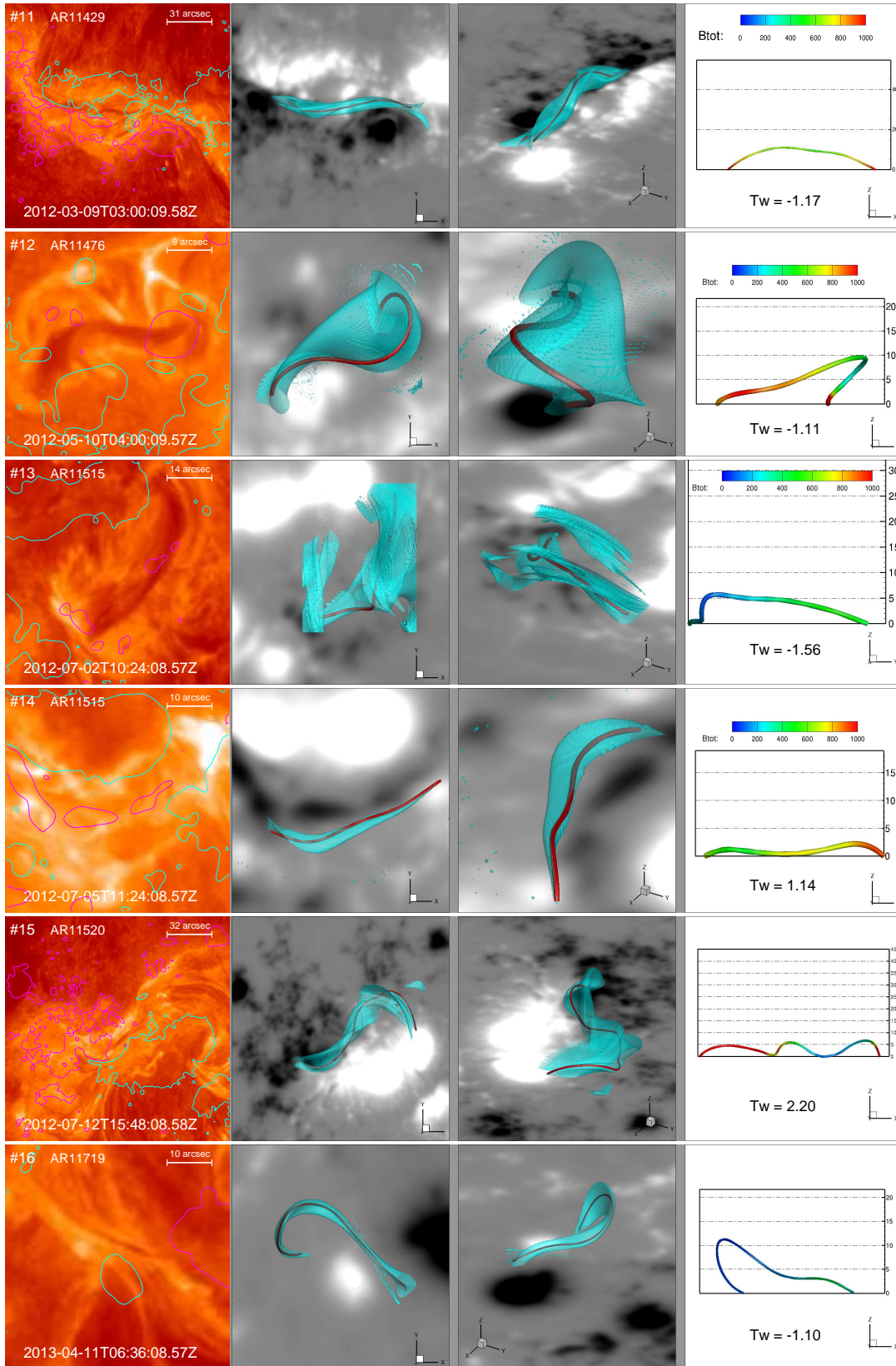
Figure 4. Same as Figure 3, but for another 6 events.
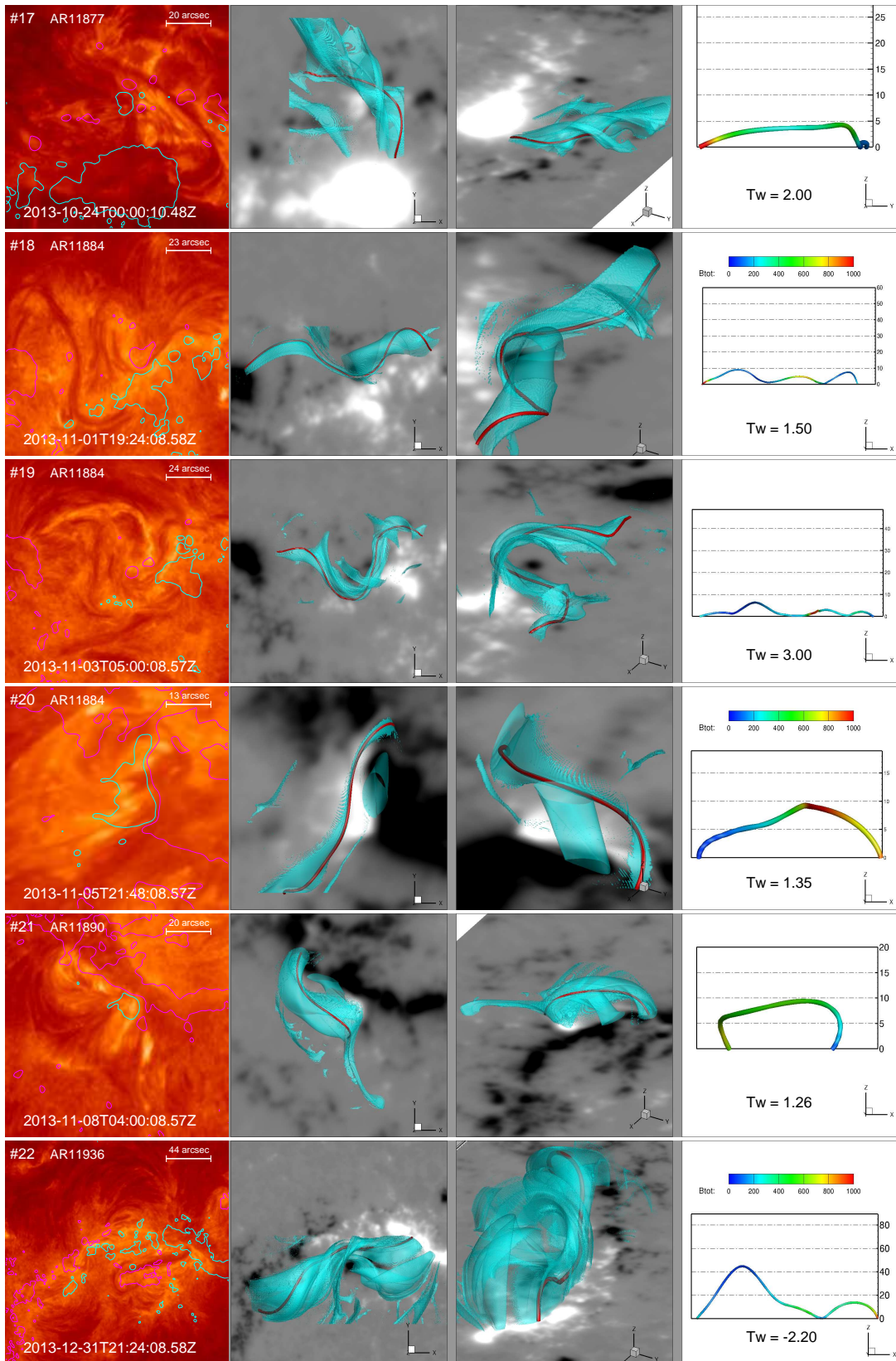
Figure 5. Same as Figure 3, but for another 6 events.
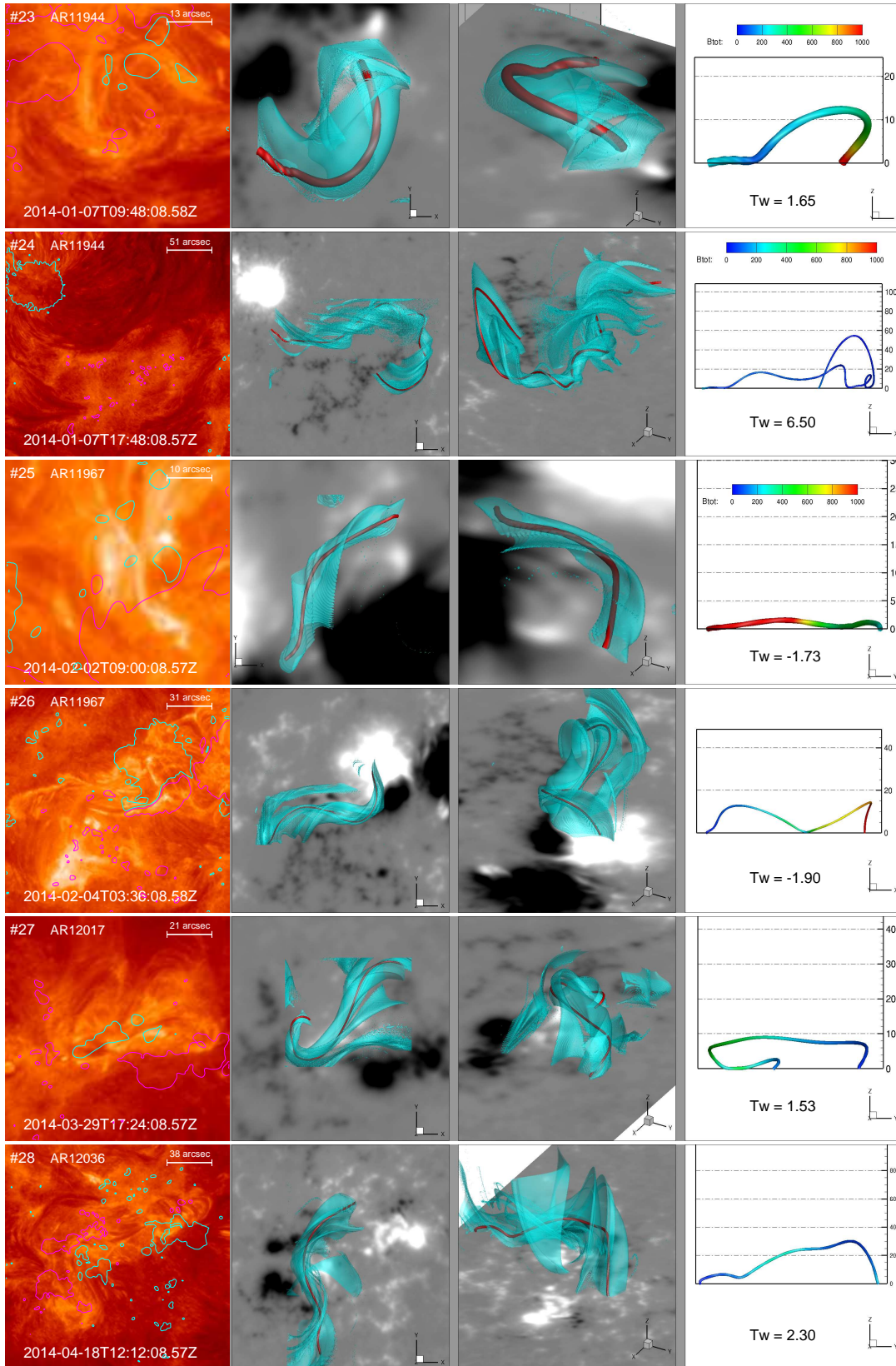
Figure 6. Same as Figure 3, but for another 6 events.
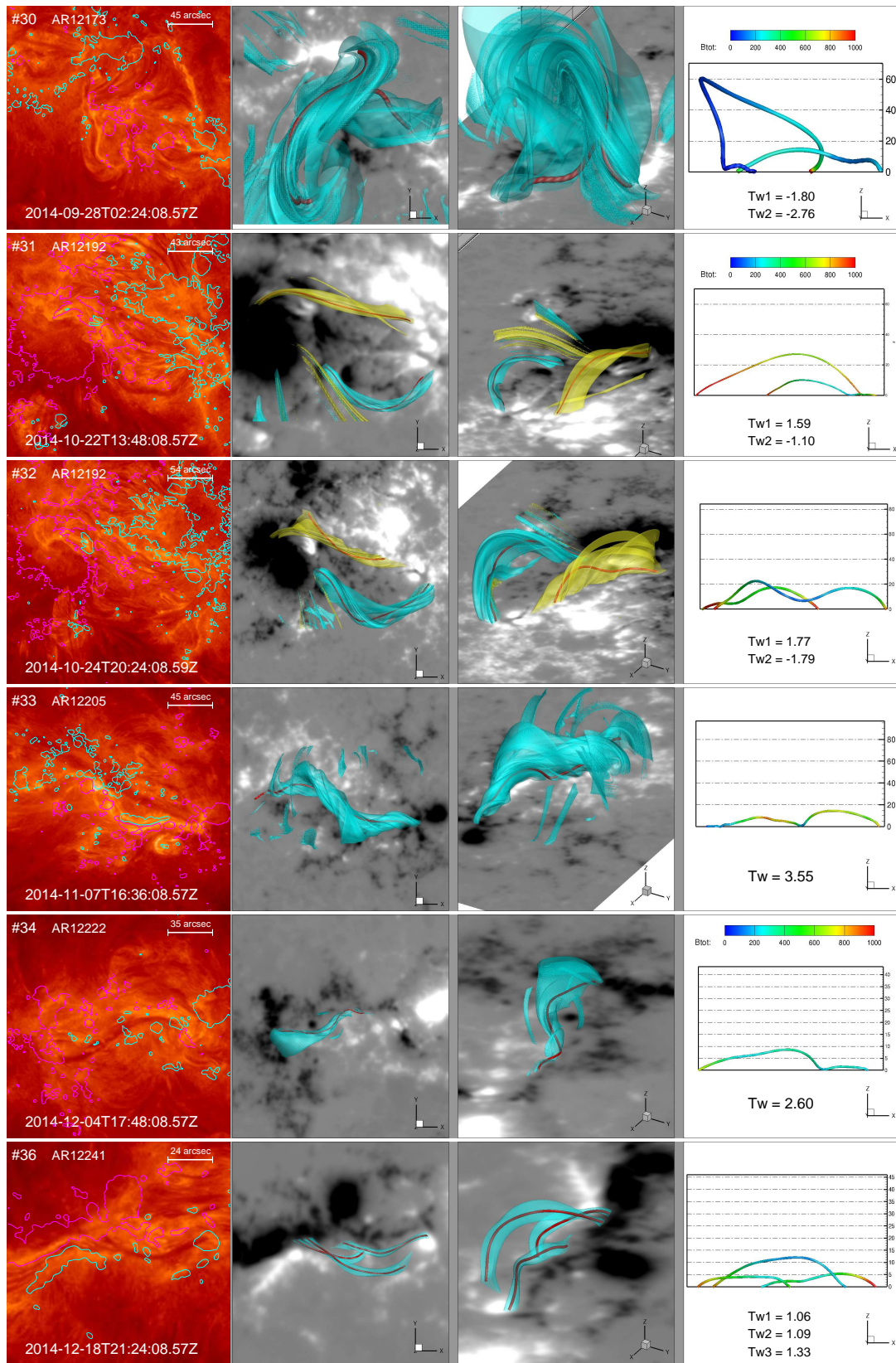
Figure 7. Same as Figure 3, but for another 6 events. Note that in events 31 and 32, the iso-surfaces of $T_w = 1$ are colored in cyan and $T_w = -1$ colored in yellow.
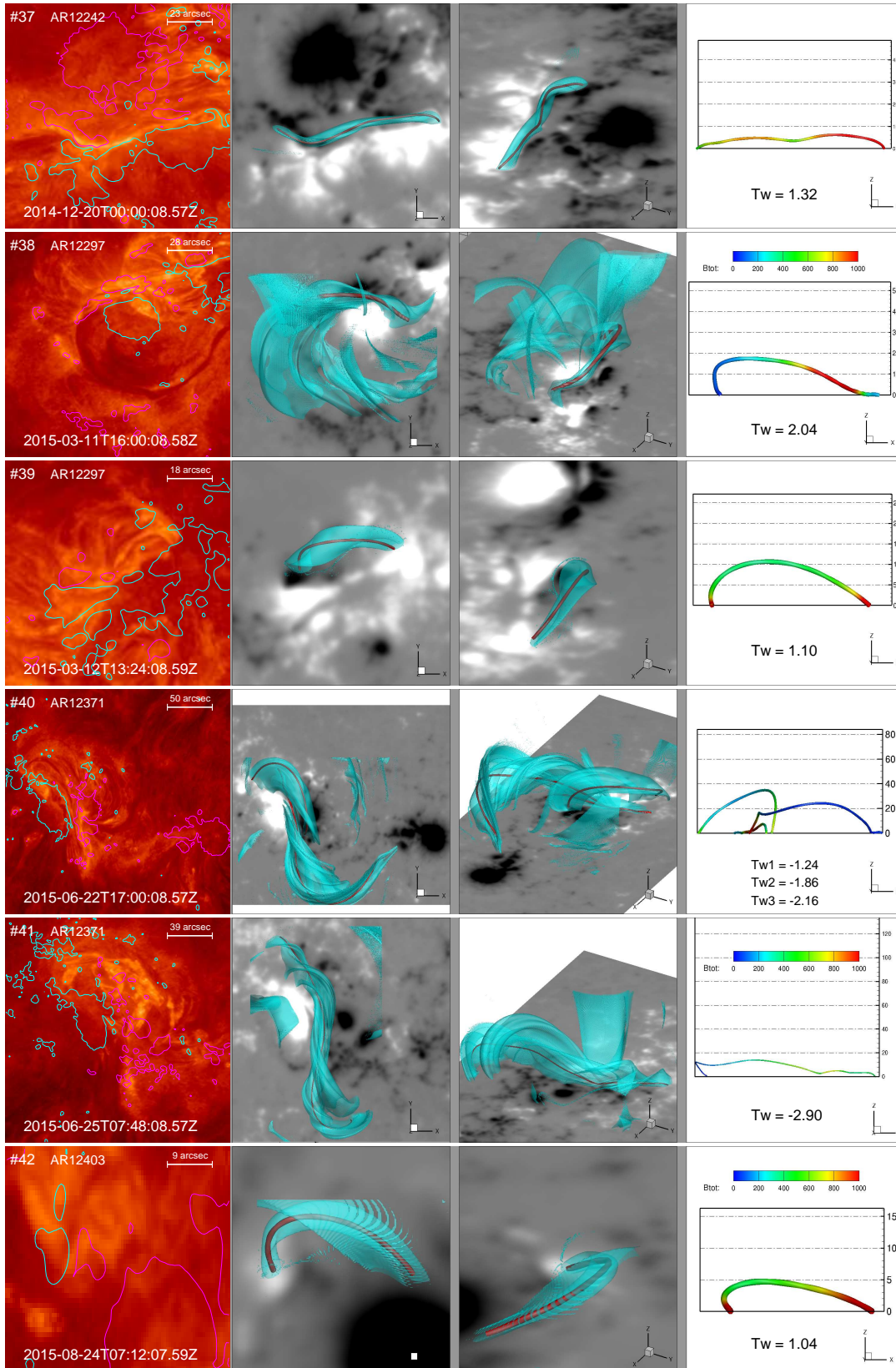
Figure 8. Same as Figure 3, but for another 6 events.
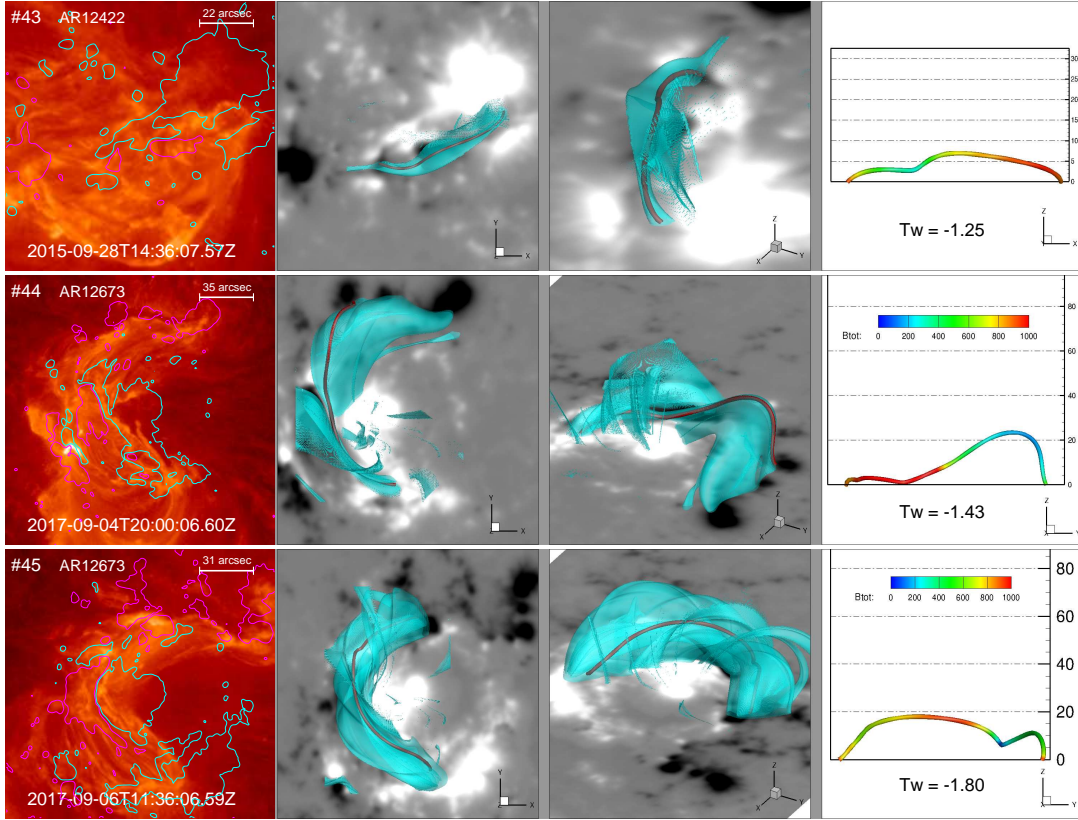
Figure 9. Same as Figure 3, but for the last 3 events.

tion for eruptive flare. For all the events with $|T_w|_{max}$ above $|T_w|_{crit}$ (i.e., in Q1+Q4), 85% erupted (11 in 13). This suggests that $n_{crit} = 1.3$ and $|T_w|_{crit} = 2$ can be reliably used as the lower limits of the threshold values for KI and TI in our statistic samples. So it is reasonable to assume that the events fall in Q1 fulfill both TI and KI, in Q2 fulfill only TI, in Q4 fulfill only KI, and in Q3 none of MHD instabilities is fulfilled. Over 87% confined events (14 in 16) reside in Q3, for which both KI and TI are not fulfilled. If doing a prediction for the type of eruptive or confined in all the 45 events using the critical values of n and $|T_w|$ derived from the pre-flare field reconstructions, over 70% are successful predicted and the remaining 13 events include 11 eruptive ones in Q3 and 2 confined ones in Q4.

The TI threshold $n_{crit} = 1.3$ is close to that derived from many theoretical models or simulations, which is $n = 1.3 \sim 1.5$. Furthermore, most of the events above n_{crit} have decay index clustered within the domain of $[1.5, 1.7]$. The average value of n for all the events above n_{crit} is $\bar{n} = 1.79$ and the standard deviation is $\sigma = 0.35$. On the other hand, since the trigger of KI depends on many parameters of MFR such as aspect ratio, the geometry of the axis, line tying, and other details of the configuration, there seems to be no single value or values in a narrow region for the KI threshold. In our statistic results, the $|T_w|_{max}$ for all eruptive events above $|T_w|_{crit}$ spread out much more than the distribution of n above n_{crit} (the av-
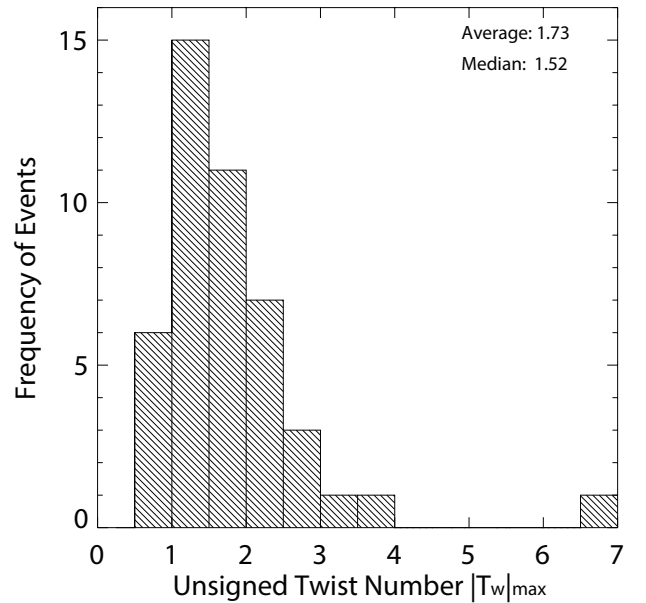
Figure 10. Histogram of the $|T_w|_{max}$ for all the MFRs. The mean and median values are denoted on the figure.

erage of $|T_w|_{max}$ is $\overline{|T_w|_{max}} = 2.82$ and the standard deviation is $\sigma = 1.31$). This agrees with the complexity in the configurations of the MFRs, and trigger of KI needs rather different threshold values depending on the details of the complex configurations. With photospheric line tying included, the min-
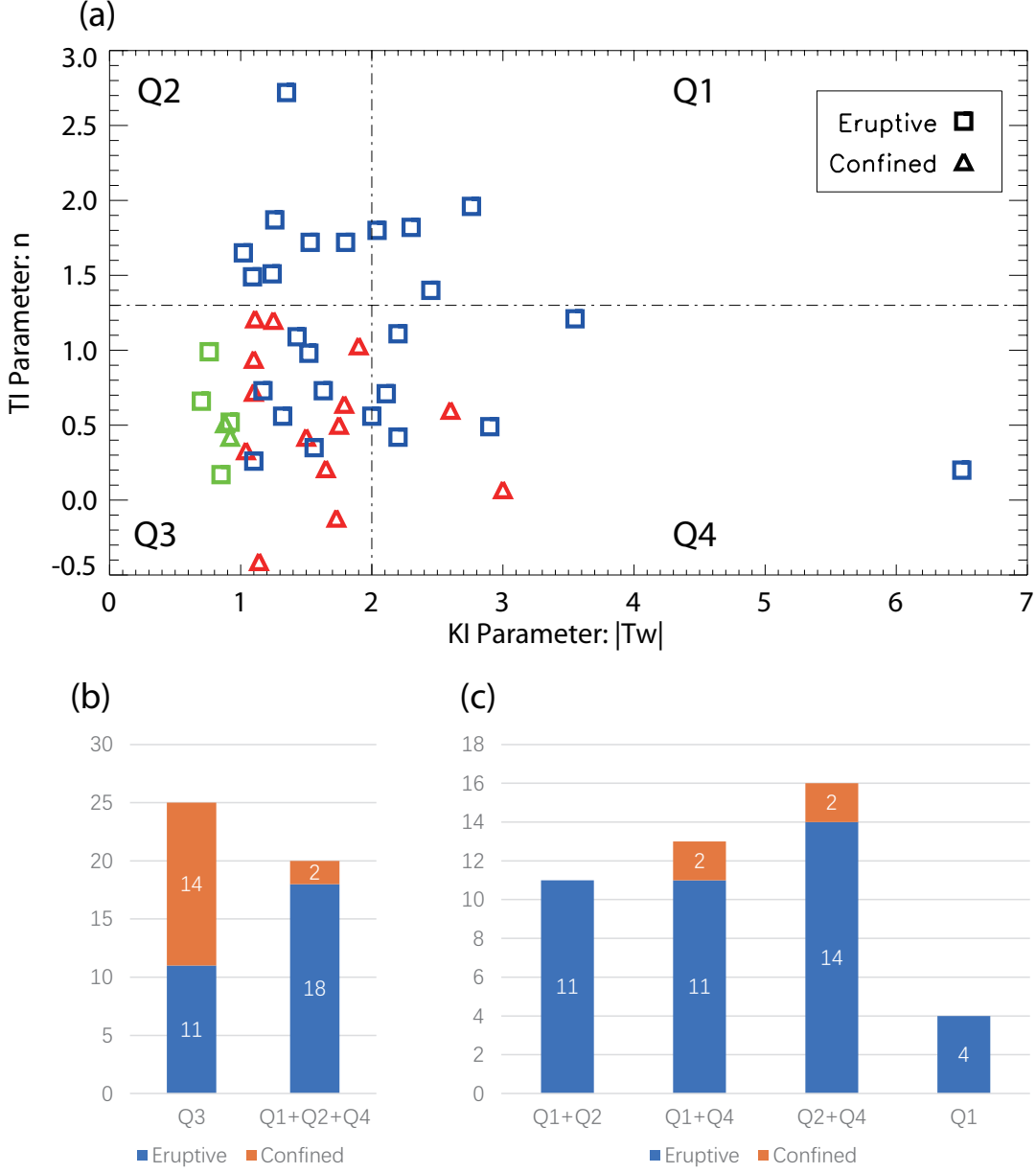
Figure 11. Scatter diagram of decay index n (TI parameter) vs. $|T_w|_{max}$ (KI parameter) and histograms of the number of different-type events. (a) The boxes denote eruptive flares and the triangles denote confined flares, while those in green color denotes the non-MFR events, i.e., $|T_w|_{max}$ is less than 1. The vertical dashed line marks the $|T_w| = 2$, and the horizontal dashed line marks the $n = 1.3$. Based on these two lines, the distribution of all the events can be divided into four quadrants, $Q1$, $Q2$, $Q3$, and $Q4$. (b) Histogram for numbers of events in $Q3$ and $Q1+Q2+Q4$. (c) Histogram for numbers of events in $Q1+Q2$, $Q1+Q4$, $Q2+Q4$, and $Q1$.

imum threshold from theory is a winding of the field lines about the rope axis by 1.25 turns (Hood & Priest 1981). Our statistic results suggests that the KI threshold is much larger than this minimum value, but the lower limit $|T_w|_{crit} = 2$ is comparable with estimations of winding number from numerical models of solar flux ropes (e.g., 1.75 in Török et al. 2004) and (1.875 in Fan & Gibson 2003).

If we assume that all the eruptive events with $n \geq n_{crit}$ are triggered by TI (i.e., events in $Q1+Q2$), and meanwhile all the eruptive events with $|T_w| \geq |T_w|_{crit}$ are caused by KI (i.e., events in $Q1+Q4$ except the two confined ones), their num-

bers are equal (see Figure 11c). This indicates that KI plays an equally important role as TI in triggering eruptions. On the other hand, the total number of the eruptive events in Q2+Q4, that is triggered by either TI or KI, is 14. This is much larger than that in Q1 (events fulfill both TI and KI) which have only 4 events, suggesting that TI and KI do not necessarily to be fulfilled simultaneously to trigger an eruption.

In summary, our analysis suggests that either of the two parameters, n and $|T_w|_{max}$, provides a strong constraint on the eruptiveness of major flares, i.e., if $n \geq n_{crit}$ or $|T_w|_{max} \geq$

$|T_w|_{\rm crit}$, the event has a very high possibility (90% in our studied samples) of successful eruption. For the remaining events with both $n < n_{\rm crit}$ and $|T_w|_{\rm max} < |T_w|_{\rm crit}$, they can either be eruptive or confined. Furthermore, their distribution in this domain (Q3) appears rather random between the eruptive and confined ones, suggesting the T_w and n, or, KI and TI, cannot differentiate the types, which hints that magnetic reconnection rather than ideal MHD instability of MFR is the flare trigger. Their total number is 25, i.e., 56% of the all events. Interestingly, there are two cases in which n is negative, because the MFR is too low that the overlying flux initially increases rather than decreases. Finally, as noted in Section 3.1 there are 4 events having no filament co-spatial with the reconstructed MFRs, which are event 16 (eruptive in Q3), 20 (eruptive in Q2 with the largest n), 25 (confined in Q3), and 43 (confined in Q3). If excluding those events, our findings remain valid with only some of the percentages changing slightly.

4. DISCUSSIONS AND CONCLUSIONS

In this paper, we carried out a survey of the MFRs existing immediately before major solar flares (generally above GOES M5 class) using a coronal magnetic field reconstruction method with *SDO*/HMI vector magnetograms. By analyzing the configurations and two key parameters, which are decay index and the maximum twist number in the MFR, for ideal MHD instabilities of MFR, we have the following key findings.

1. In consistence with many previous case studies (e.g., Rust 2003; Gibson et al. 2006; Canou et al. 2009; Green & Kliem 2009; Yeates & Mackay 2009; Canou & Amari 2010; Savcheva et al. 2015; Su et al. 2015; Yurchyshyn et al. 2015; Zou et al. 2019), MFRs generally exists prior to major solar flares. With a rigorous definition, there are over 90% of the studied events have well-defined MFRs in the flare site, i.e., a coherent group of magnetic field lines with twist above one turn and the field line possessing the peak value of twist as being the rope axis. The rest 10% events also have MFR-like structures as their magnetic twist numbers are very close to one. The maximum twist numbers in the MFRs have an average value of 1.73 for all the events, which is systematically higher than that from other reconstruction methods (e.g., Wang et al. 2016; Liu et al. 2016; Jing et al. 2018). Most of the MFRs have corresponding filaments or filament channels as seen in *SDO*/AIA 304 Å observations.

2. It is the first time that all the pre-flare MFRs of such large sample are presented with 3D configuration. The reconstructed MFRs demonstrated much more complex configurations in details than idealized models of MFR that are often used in theoretical investigations or numerical simulations (e.g., Titov & Démoulin 1999; Török & Kliem 2005; Aulanier et al. 2010; Mei et al. 2018). Furthermore, multiple MFRs are found in 20% of the events, and in a few cases (in the AR 12192), the MFRs can even have inverse signs of magnetic twist. This might provide a new way of explaining the confinement of the flares from the point of view of magnetic helicity and further investigation is required.

3. The parameter diagram formed by the twist number of the MFR axis and its decay index suggests a lower limit for TI and KI thresholds, which are $n_{\rm crit} = 1.3$ and $|T_w|_{\rm crit} = 2$, respectively. All the events above the $n_{\rm crit}$, and nearly 90% of the events above the $|T_w|_{\rm crit}$ erupted. The eruptive events above the TI threshold have an average decay index with a small deviation of 1.79 ± 0.35, which is close to many theoretical derived TI thresholds, although the reconstructed MFRs are much more complex than the theoretical ones. On the other hand, the values for KI threshold spread out in a wider domain of 2.83 ± 1.31. From this result, an important argument can be made: the KI are more sensitive to the details of the MFR itself while the TI depends mainly on decaying speed of the strapping field overlying the MFR [3].

4. Our results show significant difference from a previous similar study by Jing et al. (2018). In their findings, the lower limit of TI threshold is $n_{\rm crit} = \sim 0.75$, and the KI seems to play no role in differentiating the eruptive and confined events. On the contrary, our results show that the **TI** threshold ($n_{\rm crit}$) is much higher, and furthermore, KI is equally important as TI in producing eruption. Such difference of our results from Jing et al. (2018)'s can be attributed to many factors, and we suspect that the leading one is that different coronal field reconstruction methods were used (the Wiegelmann's code was used in Jing et al. (2018)). The inconsistence between different reconstruction codes applied to the real data has been extensively reported (e.g., DeRosa et al. 2009; Régnier 2013; Aschwanden et al. 2014; Duan et al. 2017; Wiegelmann et al. 2017), even though they can provide rather consistent results in some benchmark tests using idealized or artificial magnetograms. Furthermore, the computational method of decay index at the MFR's axis and the using of the maximum $|T_w|$ in the MFR as the KI parameter are also different from the analysis method in Jing et al. (2018). Since the results in this paper is more consistent with theoretical studies, we thus suggest that it might be more relevant to follow the approach taken here in future application of TI and KI to reconstructed coronal field. On the one hand, our definition of MFR is much stricter and the maximum of twist number of MFR is more sensitive than the average twist that includes also the contribution of the flux with $|T_w| < 1$, as such weakly twisted flux is not relevant to the MFRs. On the other hand, computing the oblique decay index is more relevant to the eruption at the early phase, i.e., its initiation due to the complex, non-

---

[3] Of course, regarding the TI, there must be a MFR before the flare, otherwise the TI is meaningless. However, this requirement seems to be often ignored in application of the TI theory to observations. This also might explains why there is a so-called 'failed torus' regime as reported in Myers et al. (2015) because in that regime the magnetic twist numbers are mostly less than one, and thus by a strict definition, the MFR barely exists.

symmetric magnetic environments.

5. Comparing to the eruptive events fulfilled either TI or KI, the events fulfilled both are minor. This suggests that TI and KI do not necessarily to be fulfilled at the same time to trigger an eruption. This is reasonable as on the one hand, the presence of a well-defined MFR (i.e., with magnetic twist number above 1) will erupt once it runs into the TI regime, and on the other hand a initially torus-stable MFR can be lifted to TI threshold through the kinking deformation of the MFR.

6. The events with both decay index and twist degree below our derived lower limits of TI and KI accounts for 56% (and among them 44% are eruptive). For these events, we conjecture that the ideal MHD instabilities might not be able to trigger the flare, and the non-ideal MHD mechanism, i.e., magnetic reconnection, should play an more important role, in particular, in producing the successful eruption. Recently, Zou et al. (2019, in press) have carried out a statistic survey for all the AR filament eruptions from 2011 to 2017 which produced fast CMEs (above 800 km s^{-1}) and found that over 60% of AR filaments are more likely triggered by reconnection rather than the ideal MHD instability. Our percentage of

56% is close to their result, which further indicates that magnetic reconnection (e.g., tether cutting and breakout) plays an important role (at least, equal to the ideal MHD instabilities) in the triggering of major flares and eruptions. Thus for understanding the mechanism of these flares, a detailed analysis of the magnetic topology that is favorable for reconnection is required. In particular, more attention should be paid on the eruptive events in the regime to see how the reconnection can break through the strong confinement of the overlying field, which will be left in future studies.

REFERENCES

Amari, T., Canou, A., & Aly, J. J. 2014, Nature, 514, 465

Antiochos, S. K., DeVore, C. R., & Klimchuk, J. A. 1999, ApJ, 510, 485, doi: 10.1086/306563

Aschwanden, M. J., Sun, X., & Liu, Y. 2014, The Astrophysical Journal, 785, 34

Aulanier, G. 2014, in IAU Symposium, Vol. 300, IAU Symposium, ed. B. Schmieder, J.-M. Malherbe, & S. T. Wu, 184–196

Aulanier, G., Török, T., Démoulin, P., & DeLuca, E. E. 2010, ApJ, 708, 314, doi: 10.1088/0004-637X/708/1/314

Bateman, G. 1978, MHD instabilities (Cambridge, MA: MIT Press,)

Baty, H. 2001, A&A, 367, 321, doi: 10.1051/0004-6361:20000412

Berger, M. A., & Prior, C. 2006, Journal of Physics A Mathematical General, 39, 8321, doi: 10.1088/0305-4470/39/26/005

Bobra, M. G., Sun, X., Hoeksema, J. T., et al. 2014, SoPh, 289, 3549, doi: 10.1007/s11207-014-0529-3

Canou, A., & Amari, T. 2010, ApJ, 715, 1566, doi: 10.1088/0004-637X/715/2/1566

Canou, A., Amari, T., Bommier, V., et al. 2009, ApJL, 693, L27, doi: 10.1088/0004-637X/693/1/L27

Chen, J. 1989, ApJ, 338, 453, doi: 10.1086/167211

Cheng, X., Guo, Y., & Ding, M. 2017, Science China Earth Sciences, 60, 1383, doi: 10.1007/s11430-017-9074-6

Cheng, X., Zhang, J., Ding, M. D., et al. 2013, ApJL, 769, L25, doi: 10.1088/2041-8205/769/2/L25

Démoulin, P., & Aulanier, G. 2010, ApJ, 718, 1388, doi: 10.1088/0004-637X/718/2/1388

DeRosa, M. L., Schrijver, C. J., Barnes, G., et al. 2009, ApJ, 696, 1780, doi: 10.1088/0004-637X/696/2/1780

Duan, A., Jiang, C., Hu, Q., et al. 2017, ApJ, 842, 119, doi: 10.3847/1538-4357/aa76e1

Fan, Y. 2010, ApJ, 719, 728

Fan, Y., & Gibson, S. E. 2003, ApJL, 589, L105, doi: 10.1086/375834

—. 2007, ApJ, 668, 1232, doi: 10.1086/521335

Forbes, T. G., Linker, J. A., Chen, J., et al. 2006, SSRv, 123, 251, doi: 10.1007/s11214-006-9019-8

Getling, A. V. 2019, arXiv e-prints. https://arxiv.org/abs/1904.08367

Gibson, S. E., Fan, Y., Török, T., & Kliem, B. 2006, SSRv, 124, 131, doi: 10.1007/s11214-006-9101-2

Green, L. M., & Kliem, B. 2009, ApJL, 700, L83, doi: 10.1088/0004-637X/700/2/L83

Guo, Y., Cheng, X., & Ding, M. 2017, Science China Earth Sciences, 60, 1408, doi: 10.1007/s11430-017-9081-x

Hood, A. W., & Priest, E. R. 1981, Geophysical and Astrophysical Fluid Dynamics, 17, 297, doi: 10.1080/03091928108243687

Inoue, S., Shiota, D., Bamba, Y., & Park, S.-H. 2018, ApJ, 867, 83, doi: 10.3847/1538-4357/aae079

Janvier, M., Aulanier, G., & Démoulin, P. 2015, SoPh, 290, 3425, doi: 10.1007/s11207-015-0710-3

Jiang, C., & Feng, X. 2013, ApJ, 769, 144, doi: 10.1088/0004-637X/769/2/144

Jiang, C., Wu, S. T., Feng, X., & Hu, Q. 2014, ApJL, 786, L16, doi: 10.1088/2041-8205/786/2/L16

Jiang, C., Wu, S. T., Yurchyshyn, V. B., et al. 2016, ApJ, 828, 62

Jiang, C., Zou, P., Feng, X., et al. 2018, ApJ, 869, 13, doi: 10.3847/1538-4357/aaeacc

Jiang, C. W., Feng, X. S., Wu, S. T., & Hu, Q. 2013, ApJL, 771, L30

Jiang, C. W., Feng, X. S., Zhang, J., & Zhong, D. K. 2010, SoPh, 267, 463

Jing, J., Liu, C., Lee, J., et al. 2018, ApJ, 864, 138, doi: 10.3847/1538-4357/aad6e4

Kliem, B., & Török, T. 2006, Physical Review Letters, 96, 255002, doi: 10.1103/PhysRevLett.96.255002

Kuperus, M., & Raadu, M. A. 1974, A&A, 31, 189

Liu, L., Cheng, X., Wang, Y., et al. 2018, ApJL, 867, L5, doi: 10.3847/2041-8213/aae826

Liu, R., Kliem, B., Titov, V. S., et al. 2016, The Astrophysical Journal, 818, 148

Low, B. C., & Lou, Y. Q. 1990, ApJ, 352, 343, doi: 10.1086/168541

McCauley, P. I., Su, Y. N., Schanche, N., et al. 2015, SoPh, 290, 1703, doi: 10.1007/s11207-015-0699-7

Mei, Z. X., Keppens, R., Roussev, I. I., & Lin, J. 2018, A&A, 609, A2, doi: 10.1051/0004-6361/201730395

Mikic, Z., & Linker, J. A. 1994, ApJ, 430, 898, doi: 10.1086/174460

Mitra, P. K., Joshi, B., Prasad, A., Veronig, A. M., & Bhattacharyya, R. 2018, ApJ, 869, 69, doi: 10.3847/1538-4357/aaed26

Moore, R. L., Sterling, A. C., Hudson, H. S., & Lemen, J. R. 2001, ApJ, 552, 833, doi: 10.1086/320559

Myers, C. E., Yamada, M., Ji, H., et al. 2015, Nature, 528, 526, doi: 10.1038/nature16188

Olmedo, O., & Zhang, J. 2010, ApJ, 718, 433, doi: 10.1088/0004-637X/718/1/433

Petrie, G. J. D. 2019, ApJS, 240, 11, doi: 10.3847/1538-4365/aaef2f

Régnier, S. 2013, Solar Physics, 288, 481, doi: 10.1007/s11207-013-0367-8

Rust, D. M. 2003, Advances in Space Research, 32, 1895, doi: 10.1016/S0273-1177(03)90623-5

Savcheva, A., Pariat, E., McKillop, S., et al. 2015, ApJ, 810, 96, doi: 10.1088/0004-637X/810/2/96

Schmieder, B., & Aulanier, G. 2012, Advances in Space Research, 49, 1598, doi: 10.1016/j.asr.2011.10.023

Schmieder, B., Démoulin, P., & Aulanier, G. 2013, Advances in Space Research, , doi: 10.1016/j.asr.2012.12.026

Seaton, D. B., & Darnel, J. M. 2018, ApJL, 852, L9, doi: 10.3847/2041-8213/aaa28e

Shibata, K., & Magara, T. 2011, Living Reviews in Solar Physics, 8, 6

Su, Y., Surges, V., van Ballegooijen, A., DeLuca, E., & Golub, L. 2011, ApJ, 734, 53, doi: 10.1088/0004-637X/734/1/53

Su, Y., van Ballegooijen, A., McCauley, P., et al. 2015, ApJ, 807, 144, doi: 10.1088/0004-637X/807/2/144

Sun, X., & Norton, A. A. 2017, Research Notes of the American Astronomical Society, 1, 24, doi: 10.3847/2515-5172/aa9be9

Sun, X., Bobra, M. G., Hoeksema, J. T., et al. 2015, ApJL, 804, L28

Titov, V. S., & Démoulin, P. 1999, A&A, 351, 707

Toriumi, S., Schrijver, C. J., Harra, L. K., Hudson, H., & Nagashima, K. 2017, ApJ, 834, 56, doi: 10.3847/1538-4357/834/1/56

Török, T., Berger, M. A., & Kliem, B. 2010, A&A, 516, A49, doi: 10.1051/0004-6361/200913578

Török, T., & Kliem, B. 2003, A&A, 406, 1043, doi: 10.1051/0004-6361:20030692

—. 2005, ApJL, 630, L97, doi: 10.1086/462412

—. 2007, Astronomische Nachrichten, 328, 743, doi: 10.1002/asna.200710795

Török, T., Kliem, B., & Titov, V. S. 2004, A&A, 413, L27, doi: 10.1051/0004-6361:20031691

Wang, H., Yurchyshyn, V., Liu, C., et al. 2018, Research Notes of the AAS, 2, 8

Wang, Y., Zhuang, B., Hu, Q., et al. 2016, Journal of Geophysical Research (Space Physics), 121, 9316, doi: 10.1002/2016JA023075

Wiegelmann, T. 2004, SoPh, 219, 87, doi: 10.1023/B:SOLA.0000021799.39465.36

Wiegelmann, T., Petrie, G. J. D., & Riley, P. 2017, SSRv, 210, 249, doi: 10.1007/s11214-015-0178-3

Yeates, A. R., & Mackay, D. H. 2009, ApJ, 699, 1024, doi: 10.1088/0004-637X/699/2/1024

Yurchyshyn, V., Kumar, P., Cho, K.-S., Lim, E.-K., & Abramenko, V. I. 2015, ApJ, 812, 172, doi: 10.1088/0004-637X/812/2/172

Zou, P., Jiang, C., Feng, X., et al. 2019, ApJ, 870, 97, doi: 10.3847/1538-4357/aaf3b7

Zuccarello, F. P., Aulanier, G., & Gilchrist, S. A. 2015, ApJ, 814, 126, doi: 10.1088/0004-637X/814/2/126